An experimental and numerical study of the effects of length scale and strain state on the necking and fracture behaviours in sheet metals

P. Hogström, J.W. Ringsberg, E. Johnson

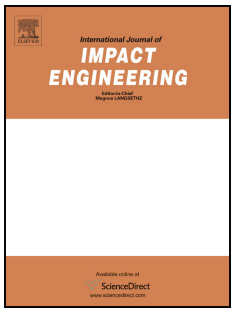

Title: An experimental and numerical study of the effects of length scale and strain state on the necking and fracture behaviours in sheet metals

Authors: P. Hogström, J.W. Ringsberg, E. Johnson

PII: S0734-743X(09)00091-8

DOI: 10.1016/j.ijimpeng.2009.05.005

Reference: IE 1778

To appear in: *International Journal of Impact Engineering*

Received Date: 17 December 2008

Revised Date: 11 May 2009

Accepted Date: 11 May 2009

Please cite this article as: Hogström P, Ringsberg JW, Johnson E. An experimental and numerical study of the effects of length scale and strain state on the necking and fracture behaviours in sheet metals, International Journal of Impact Engineering (2009), doi: 10.1016/j.ijimpeng.2009.05.005

An experimental and numerical study of the effects of length scale and strain state on the necking and fracture behaviours in sheet metals

P. Hogström[1,*], J.W. Ringsberg[1] and E. Johnson[2]
[1]Department of Shipping and Marine Technology,
Chalmers University of Technology, Göteborg, Sweden
[2]SP, Technical Research Institute of Sweden, Borås, Sweden
[*]Corresponding author. E-mail: Per.Hogstrom@chalmers.se

Abstract

Within sheet metal forming, crashworthiness analysis in the automotive industry and ship research on collision and grounding, modelling of the material failure/fracture, including the behaviour at large plastic deformations, is critical for accurate failure predictions. In order to validate existing failure models used in finite element (FE) simulations in terms of dependence on length scale and strain state, tests recorded with the optical strain measuring system ARAMIS have been conducted. With this system, the stress-strain behaviour of uniaxial tensile tests was examined locally, and from this information true stress-strain relations were calculated on different length scales across the necking region. Forming limit tests were conducted to study the multiaxial failure behaviour of the material in terms of necking and fracture. The failure criteria that were verified against the tests were chosen among those available in the FE software Abaqus and the Bressan-Williams-Hill (BWH) criterion proposed by Alsos et al. 2008. The experimental and numerical results from the tensile tests confirmed that Barba's relation is valid for handling stress-strain dependence on the length scale used for strain evaluation after necking. Also, the evolution of damage in the FE simulations was related to the processes ultimately leading to initiation and propagation of a macroscopic crack in the final phase of the tensile tests. Furthermore, numerical simulations using the BWH criterion for prediction of instability at the necking point showed good agreement with the forming limit test results. The effect of pre-straining in the forming limit tests and the FE simulations of them is discussed.

Keywords: Digital Image Correlation (DIC); Finite element analysis; Forming limit test; Length scale dependence; Sheet metal failure; Tensile test.

1. Introduction

Sheet metal forming processes, crashworthiness in the automotive industry, and ship collision and grounding are examples of areas in which numerical models play an important role in process development, in the design of full-scale tests/prototypes, and as a substitution for full-scale tests. The finite element (FE) method is an established numerical tool suitable for these purposes. However, there is still a need to continuously study, improve and validate the influence of many parameters in the numerical simulations and models due to ever increasing demands for more accurate predictions of, for example, material failure or for mimicking the responses recorded in tests that have been carried out. Often, both the accuracy and reliability of numerical models and what they aim to represent are discussed, together with whether or not their applicability is general or limited to specific conditions or types of analyses, see Alsos et al. [1].

This investigation focuses on the analysis of structures made of thin steel sheets considering their structural resistance to fracture as a result of large plastic deformations caused by, as one example, a collision between two cars or two ships. The objective was to analyze and compare models for material failure using an explicit FE software. Results from FE simulations are compared with experimental results from uniaxial tensile tests and forming limit (FL) tests. Consequently, the influence of the element size of the mesh, the length scale dependence on the failure limit and damage evolution models can be studied in detail. Additional topics that are addressed are the influence of multiaxial strain state on failure (see Alsos et al. [1]) and the applicability and reliability of the criteria studied in numerical investigations of ship-ship collision events. The most frequently used criteria for predicting material failure are based on effective

plastic strain. Such criteria have gained popularity due to their simple and effective formulation and have proven to give results with satisfying accuracy by Karlsson et al. [2], among others. However, these criteria neglect the influence of strain state, and recently, criteria which take this into account have been proposed and applied, see e.g. Hong et al. [3]. An example of such a criterion, which was compared with the experiments, is the Bressan-Williams-Hill (BWH) criterion proposed by Alsos et al. [1] in 2008.

In the experiments, the ARAMIS optical strain measuring system [4] was used, which enabled accurate monitoring of displacements on the specimen surfaces. A brief description of this system is given in Section 2. When a material reaches the limit of its capacity to carry further loading, deformations localize into necking and become highly dependent on the length over which the strain evaluation is performed – the length scale. In FE simulations, this length scale dependence must be taken into account when using elements of different sizes in the mesh, as discussed by Lehmann and Peschmann [5] and Hong et al. [3]. This issue, as well as the applicability of Barba's relation, are addressed in Section 3. Furthermore, the strain axiality also has an impact on the necking and fracture behaviour of the material which should be accounted for in FE simulations. These effects can be investigated with information from FL tests as discussed by Ramaekers [6], Ragab [7], Zhao et al. [8], and Stoughton and Zhu [9]. This type of test is described in Section 4. In Section 5, an analytical solution of the BWH criterion [1] is presented and applied on the forming limit test results. The capacity of some failure criteria available in the FE software Abaqus/Explicit is investigated in Section 6. This section also presents the results from the FE simulations of the tests. Note that throughout the current investigation stresses and strains are always the true stresses and strains unless otherwise stated.

2. The ARAMIS system and the material tested

The optical strain measuring system ARAMIS [4] was used in the tests to make precise measurements of the displacements on the surface of the specimens tested. The measuring system consists of two digital cameras connected to a computer with an image recognizing software matching the images from the cameras. Based on these images, the ARAMIS system can identify points on the specimen surface and divide it into facets (pixels). The distortion of these facets is monitored throughout a test in three-dimensional space. Prior to the tests, a thin coating with a stochastic pattern, which the ARAMIS system uses to identify facets and follow their displacements, was added to the specimen's surface. The random pattern on the surface of the specimen was used to follow the deformation as well as fracture behaviour of the specimen material. The resulting facet displacement shows, for instance, regions of localized strains. The accuracy in the results of displacements given from the ARAMIS system depends greatly on the size of the test specimen and the test setup. The manufacturer claims the accuracy of displacement measurement to be in the interval 0.01 – 0.1 pixels. In the test setup of the current study, the size of the pixels was 0.05 mm, giving an accuracy of at least 0.005 mm. The cameras used in the present study allow for a constant sampling frequency of 1 Hz, and the computer used has the capacity to store up to 500 images during one test.

Three materials were tested in the current investigation: the NVA mild steel [10], the Domex 355 high strength steel [11], and the NV5083 aluminium material [10]. The NVA material is a material that is commonly used in shipbuilding today, while the frequency of use of Domex 355 and NV5083 materials have increased lately as a consequence of the demands on weight reduction and lighter ship structures. The thickness of the specimens was 4 mm, and they were manufactured from hot-rolled steel plates and cold-rolled aluminium plates. The

experimental setup fulfilled the requirements in the ISO 12004-2 standard [12] and the DNV rules [10].

3. Tensile tests

The tensile tests were conducted in accordance with the DNV rules [10] but with the exception that the restriction of loading speed in the elastic region was disregarded. This was done because the elastic behaviour of the material was not a focus of the current study. Instead, the speed was set to give as high resolution in time as possible throughout the test given the sampling frequency and ability to store output data of the ARAMIS system, see Section 2. According to Dowling [13], mild steel materials similar to the NVA grade used in the current investigation may have an engineering fracture strain of up to 40%. The gauge length of the test specimen was 78 mm [10], which, with a speed of 5 mm/min in the test, allowed for an engineering strain of up to 50% at the end of the test. Fig. 1 shows the engineering stress-strain curves for the different materials from the tests. Note that there was some margin between the largest engineering strain in the test and the maximum limit of 50% strain.

Fig. 1: Typical engineering stress-strain curves for the tested materials, NVA, Domex 355 and NV5083

Fig. 2 shows the test setup for the tensile test. In order to have full control of movements out of the plane, two reference plates were introduced in the experimental setup: one was fixed to the machine foundation, and the other plate followed the moving crosshead of the tensile test machine. The specimens were manufactured according to the DNV rules [8], oriented with the loading direction aligned with the rolling direction of the sheet panel they were

manufactured from. Thus, the specimens were slightly curved prior to the test. Since the ARAMIS system only measures displacements on one surface of the test specimen, the system cannot distinguish between straightening of the specimen and its cross-sectional area contraction. However, by studying the reference plate attached to the moving crosshead of the tensile test machine, a distinction between these effects could be made: while the test specimen was undergoing elastic deformation, a slight rotation of the reference plate could be seen. Around the point of plastic yielding this rotation ceased, indicating that the test specimen had been straightened by the machine during the elastic deformation. By assuming that the area contraction of the test rod was small at this point, the area calculated there could be used as the initial area in the stress calculations. The "Aramis" stress in Fig. 3 was calculated using the force recorded by the load cell in the test machine divided by the actual area of the cross-section where fracture eventually occurred. This area was calculated using the displacement information recorded on the specimen. In Figs. 3a, 3c and 3e, the stress-strain relationships obtained from the tensile tests carried out on the NVA, the Domex 355 and the NV5083 materials are presented.

Fig. 2: Test setup for the tensile test.

The data obtained from the ARAMIS recordings allow for an analysis of the displacements over length scales defined by the engineer. As a result, the "Aramis" strain of the test rod can be measured using virtual extensometers (VE), which represent various length scales. A VE is defined as the distance between two points along the length of the test rod positioned at an equal distance from the point of fracture. A long VE corresponds to a strain value measured over the entire length of the test rod (see the bold line in Figs. 3a, 3c and 3e), while a small value of the VE corresponds to more local strain behaviour (see the dotted lines in Figs. 3a, 3c

and 3e). Traditionally, necking is identified as the point in the engineering stress-strain diagram where the stress reaches its maximum. See the vertical line in Figs. 3a, 3c and 3e for their corresponding true strain values. Another definition which is used here is the point in the true stress-strain diagram where the different VEs diverge, i.e. when the strains localize. Note that the two definitions of necking show good resemblance.

The curves fitted to the fracture points in Figs. 3b, 3d and 3f are a relation with one asymptote in the global fracture strain for the whole test rod and one asymptote where the length of the virtual extensometer approaches zero. This is known as Barba's relation and in the current investigation a formulation proposed by Yamada et al. [14] was used. It expresses the fracture strain as:

$$\varepsilon_f = \ln\left(e^{\varepsilon_n} + c\frac{\sqrt{Wt}}{L_{VE}} \right) \tag{1}$$

where e is the mathematical constant defined as the base of the natural logarithm, W is the original width of the specimen (25 mm), t is its original thickness (4 mm), ε_n is the necking strain (0.22), and L_{VE} is the VE length over which the fracture strain is measured. The Barba parameter, c, was calibrated to obtain a curve that matches the results obtained from the experiments. A comparison of the c-values for the materials shows that the higher the ultimate elongation of a material, the larger the value of c, as seen in Figs. 3 and 4.

Fig. 3: Results from the tensile tests where the stress is calculated based on the actual area of the test specimen, and the strain is measured in accordance with the length of the virtual extensometer (given in mm): **(a)** the NVA material, **(c)** the Domex 355 material and **(e)** the

NV5083 material. Presentation of the fracture strain as a function of the length of the virtual extensometer together with Barba's relation fitted to the measured points. **(b)** the NVA material, **(d)** the Domex 355 material and **(f)** the NV5083 material.

Fig. 4: Three tensile test rods after testing which are made of the NVA, the Domex355 and the NV5083 grade materials.

4. Forming limit tests

Forming limit tests were conducted to study the multiaxial strain behaviour of the material in terms of necking and fracture. The tests were limited to the NVA steel grade, which was selected because it is the most commonly used material in shipbuilding of the three materials studied in the current investigation. The tests were carried out in accordance with the ISO 12004-2 standard [12], and the ARAMIS system [4] was used to monitor the surface displacements of the test specimens. Six different geometries were tested, shown in Fig. 5a, corresponding to six data points in the forming limit diagram (FLD). Three samples of each geometry were tested. The specimens were manufactured from the same sheet panel as the tensile test specimens with the orientation of the rolling direction perpendicular to the major principal strain direction of the test section of the specimen. They were clamped by bolts in the fixture and deformed quasi-statically normal to their plane using a half spherical punch with a diameter of 100 mm, see the test setup in Fig. 5b. A lubrication layer consisting of three layers of silicon grease and two sheets of reinforced Teflon was added between the test specimen and the punch in order to reduce the influence of friction. According to standard [12], the velocity of the punch should be 1.5 ± 0.5 mm/s. However, a velocity of 0.1 mm/s was used instead because it gives a higher resolution in time of the results as determined by the sampling frequency of the cameras of the ARAMIS system (see Section 2). A low

velocity is also beneficial to reduce the influence from strain rate effects (note that strain rate effects were not incorporated in the current study).

Fig. 5: (a) The six test geometries: each of them corresponds to one strain state in the forming limit diagram. Geometry 1 is the circular plate (upper left) and geometry 6 is the narrowest of the geometries (lower right). **(b)** Test setup: the punch goes into the hold in which the specimen is clamped, the Teflon lubrication sheets can be seen between them. Also, the displacement gauge can be seen fixed on top of the punch.

The identification of the location of necking and fracture in a specimen and when it occurs during the test was determined in accordance with the ISO 12004-2 standard [12], and Fig. 6 shows an example of results in a diagram that was used for this purpose. The procedure behind the determination of fracture is presented first, followed by necking.

In the time step preceding fracture of a test specimen, the major principal strain, ε_1, in five sections perpendicular to the crack was calculated using the information from facet displacements recorded by the ARAMIS system. One section was put in the middle of the crack with two sections on each side, approximately 2 mm apart. The dots in Fig. 6 show an example of typical results in one section of a test geometry for the major principal strain. The ISO 12004-2 standard [12] prescribes that the strain values close to the crack should be excluded in the evaluation, i.e. the strain values that form the peak in Fig. 6 should be omitted in the assessment. Instead, ten strain values on each side of the crack, represented here by the squares in Fig. 6, should be used to fit an inverse second-degree-polynomial, shown by the solid line in Fig. 6. Once this polynomial has been obtained, the major principal strain of the section under consideration is defined as the peak value of the polynomial, represented by the

triangle in Fig. 6. As a result of using this method, one major principal strain value for each of the five sections is obtained. The mean value of them is the major principal strain for fracture of the test specimen. The minor principal strain, ε_2, is evaluated similarly at the time step which defines the major principal strain, ε_1, at fracture.

Fig. 6: Example of evaluation procedure of the forming limit test results in accordance with ISO 12004-2 [10] to obtain the major principal strain, ε_1, in one of the five evaluation sections of a test specimen. The position 0 along the test section (x-axis) corresponds to the location of the crack.

Necking can be defined as a localization of displacements (see Hill [15]). Utilising this definition together with the measurement data from the ARAMIS system, a methodology is proposed as to how to calculate the principal strains at necking. It partly follows the methodology prescribed by the ISO 12004-2 standard [10], but some additional steps had to be developed and incorporated for clarity and to ensure quality of the results. The specimen under consideration was divided into five sections, perpendicular to the crack, for evaluation in accordance with the ISO 12004-2 standard [10]. In every section, the major and minor principal strains were calculated in the facets using the measurement data from the ARAMIS system. These strains were also calculated as a function of time; see Fig. 7 for an example of the major principal strain in one section of a test geometry. The diagram presented in Fig. 7 was used to identify where localization takes place in the specimen, depicted by the dashed line. Following the same procedure as described in the previous paragraph for fracture principal strains, ten points on each side of the dashed line were chosen for evaluation of the characteristics of the principal strains, such as the square symbols in Fig. 6. The time history

of the evolution of the principal strains at these points was of main interest in the evaluation of necking principal strains.

For the given geometries and loading conditions of the present investigation, the major principal strain was considered to be the driving strain parameter in the evolution of localization of displacements. Fig. 8a shows an example of the time history of the major principal strain for the twenty points (cf. the squares in Fig. 6) used in the assessment in one section of a test specimen. The solid line is the standard deviation between these data as a function of time. It may serve as an indicator for when localization (i.e. necking) has already occurred by its exponential increase. In order to define necking in time, the acceleration of the principal strain (second-order derivative of principal strain) was chosen as a measure. In Fig. 8b, the major principal strain acceleration curves corresponding to the curves in diagram Fig. 8a are presented. The solid line is the standard deviation of the major principal strain acceleration curves and can be described by Eq. (2):

$$Q(t)=\left(\frac{1}{q-1}\sum_{i=1}^{q}\left(\frac{d^2\varepsilon(t)_{1,i}}{dt^2}-\frac{1}{q}\sum_{j=1}^{q}\frac{d^2\varepsilon(t)_{1,j}}{dt^2}\right)^2\right)^{1/2} \tag{2}$$

where q is the number of points in the assessment (here, q = 20), and $\varepsilon(t)_{1,i}$ and $\varepsilon(t)_{1,j}$ are the major principal strains in these points. As necking can be considered to occur almost instantaneously (or very rapidly), the point in time when the standard deviation increases significantly was used as a definition of necking, represented by the dashed line in Fig. 8b. At this point in time, a procedure similar to the definition of principal strains at fracture according to standard [12] was used: the ten points (facets) on each side of the dashed line in Fig. 7 (cf. the crack and squares in Fig. 6) were used to fit an inverse second-degree-

polynomial, which, finally, after evaluation of all of the five sections of the specimen, gives the principal strain values for necking.

Fig. 7: Example of a presentation of the evolution in time of the major principal strain in one section of a test geometry. The dashed line indicates where in the specimen localization is expected to occur.

Fig. 8: (a) Curves for the major principal strain history in the points of the evaluation window (see squares in Fig. 5) and their standard deviation enhanced by a factor of 10. **(b)** Major principal strain acceleration of the curves in (a) and their standard deviation enhanced by a factor of 10. The dashed line indicates necking.

The summary of the results from the forming limit tests are presented in the principal strain space in Fig. 9. Here, the mean values of each specimen are presented, and the error bars denote the standard deviations in test results between test specimens for the test geometries 1 to 6, respectively. It should be noted that even though the evaluation procedure [12] is designed to reduce the scatter [10], there is larger scatter in results from the measurements for fracture in the ε_1 direction in contrast to the ε_2 direction.

Fig. 9: Results from forming limit tests of the six geometries (based on three test samples per geometry with five sections on each sample): mean values and standard deviations (denoted by the error bars) in the principal strain space (ε_1 and ε_2 directions) for necking and fracture.

When establishing a strain based FLD, proportional strain path has to be assumed [6, 8, 9]. However, since the forming limit curve (FLC) is not only dependent on the material but also

the loading situation and geometry, a straight strain path is rarely the case in experiments, as concluded by Ramaekers [6]. Zhao et al. [8] performed FL tests on sheet material with different induced pre-straining using a similar test setup as the present study, showing that the pre-straining has a significant impact on the strain path. The strain paths in their experiments on rolled material show the same tendency as the FL tests, an example of which can be seen in Fig. 10 in which the strain paths of the five evaluation sections of one specimen of geometry 4 are shown. Strain in the minor principal direction comes towards the end of the test, mainly after the point of necking, giving the curvature in strain path. It may also be seen for the other geometries in Fig. 9 where the points representing necking are gathered closely together for geometries 2-6. Geometry 1 does not show this behaviour since it is fixed around its circumference. Zhao et al. [8] showed that strain paths differ between materials with different induced pre-strain, which indicates that the curvature in strain path lies within the pre-straining rather than the test setup in the present case. Stoughton and Zhu [9] argue in favour of using a stress based FLD in order to remedy the strain path dependency of the strain based FLD. However, going from a strain based to a stress based FLD requires some calculations based on assumptions. Thus, the comparison between experimental and numerical results are made in the strain based FLD in which the experimental results can be directly determined from the displacements measured by the ARAMIS system.

Fig. 10: Strain path during the forming limit tests for five sections of one test specimen geometry 4.

5. Description of a forming limit curve using the BWH criterion

Alsos et al. [1] have proposed a criterion for the onset of instability (necking) in sheet metal, which is referred to as the BWH criterion. It searches for local instability and applies only to

membrane stresses and strains, i.e. bending is disregarded in this criterion. It is described in Eq. (3) on a stress-based form:

$$\sigma_1 = \begin{cases} \dfrac{2K}{\sqrt{3}} \dfrac{1+0.5\beta}{\sqrt{\beta^2+\beta+1}} \left(\dfrac{2}{\sqrt{3}} \dfrac{\varepsilon_{1c}}{(1+\beta)} \sqrt{\beta^2+\beta+1} \right)^n, & \text{if } \beta \le 0 \\ \dfrac{2K}{\sqrt{3}} \dfrac{\left(2\varepsilon_{1c}/\sqrt{3}\right)^n}{\sqrt{1+\left(\beta/(2+\beta)\right)^2}} & \text{otherwise} \end{cases} \tag{3}$$

here, $\beta = \dot{\varepsilon}_2 / \dot{\varepsilon}_1$, K is the material strength coefficient, n is the strain hardening exponent [13] and ε_{1c} is the local necking in a uniaxial strain state. The ε_{1c} parameter is the major principal strain at the onset of necking where the FLC crosses the major principal strain axis. Examining the points of necking in the FLD in Fig. 9 reveals that a curve fitted to these points crosses the major principal axis at $\varepsilon_1 \approx 0.27$. In the current study, the strain hardening exponent, n, was obtained by a curve fit of the power stress-strain relationship to the tensile test results to $n = 0.22$. With this value and $\varepsilon_{1c} = 0.27$, the BWH curve on the strain-based form in Fig. 11 fits the test results well.

Fig. 11: Results (necking) from forming limit tests together with the analytical solution of the BWH criterion fitted to the experimental values presented in principal strains.

When going from a stress to a strain based formulation of the BWH criterion, some assumptions have to be made, such as the plane stress state along with a formulation of effective stresses (von Mises equivalent stresses and strains have been used here). In order to express a relationship between principal strains, proportional strain paths of each geometry point in the FLD, expressed as constant $\beta = \dot{\varepsilon}_2 / \dot{\varepsilon}_1 = \varepsilon_2 / \varepsilon_1$ throughout the test, are assumed

[1]. The investigation and discussion of strain paths presented in Fig. 10 indicates that this assumption may not be valid in the initial path preceding necking. Nevertheless, because experimental results are in the strain space and the deviation from proportional strain path in Fig. 10 is small compared to similar investigations (e.g. Zhao et al. [8]), the assumption of constant β was used.

6. Finite element simulations and results

The finite element model of the test specimens used in the tensile and forming limit tests consisted of shell elements with reduced integration (S4R in Abaqus/Explicit) and five section points through their thickness. Generally, shell elements that are thick in relation to their side lengths give poor results in bending; this type of element has a plane stress formulation and thus they are unable to resolve stress gradients in their thickness direction. In the uniaxial tensile tests, no bending is present. In the forming limit tests, membrane and bending stresses are present, but the membrane stresses are regarded as being dominant, making the use of shell elements feasible. In addition, results in the elements are taken in the through-thickness mid section point, i.e. in the neutral axis, and thus bending stresses are disregarded.

The material modelled was the NVA grade material represented by an isotropic hardening model with piecewise linear isotropic hardening characteristics for the plastic behaviour. A Young's modulus of 210 GPa and a yield stress of 310 MPa were used, as shown in Fig. 2a. In the simulation of the forming limit tests, zero friction was assumed, and the contact conditions between the punch and the specimen were modelled using the "general contact condition" in Abaqus/Explicit. Only half of the test specimens were modelled because of symmetry.

For the modelling of different physical phenomena leading to failure of a material, Abaqus/Explicit offers several models that handle initiation and evolution of damage. For damage initiation (DI) in ductile metals [16], either the ductile criterion, a phenomenological model for the nucleation, growth and coalescence of voids, or the shear criterion, which models shear band localization, may be used. In the current investigation, the ductile criterion was used to model the damage initiation in the FE simulation of the tensile tests using the necking strain from the tests, $\varepsilon_n = 0.22$, as the plastic strain at the onset of damage. In addition to these models, several criteria for simulating instability of sheet metal are available, such as the "FLD criterion" that was used in the simulation of the forming limit tests [16]. In Abaqus/Explicit, criteria for sheet steel can only be used with elements that have a plane stress formulation, i.e. shell, beam or truss elements.

After the damage initiation, a damage evolution model describes the degradation of the material up to the point of fracture. In Abaqus/Explicit, the evolution is defined either through the displacement at fracture, u_f, or the energy dissipated during the failure process, G_f. The former alternative was used in the current study. The displacement at fracture is defined as $u_f = L \times \varepsilon_f$ where L is a characteristic element length, and ε_f is the plastic strain at fracture taking into account the influence of the length scale, cf. Eq. 1. In the post-necking region, the element size of the mesh has a great influence on the solution (see the discussion in Section 3). Consequently, this dependency has to be accounted for when the damage evolution parameter is defined. In Abaqus/Explicit, damage evolution may be defined as linear, bilinear/piecewise linear, or following an exponential behaviour.

6.1 Finite element simulations of the tensile tests

The FE simulations of the tensile tests were conducted in order to study the damage evolution law in terms of mesh dependency (element size or length scale) and choice of damage evolution function. Several element sizes (between 2 and 8 mm) were compared to investigate its influence on the solution and results. Up to the point of damage initiation, no dependence from the element size could be seen between different FE models and simulations. However, after the initiation of damage, the influence from the element size became significant. This could be compensated for by using Barba's law by adjustment of the u_f-parameter according to the characteristic element length in the FE model, as seen in the previous section.

The stress-strain curve in Fig. 12a that represents the experiments was plotted up to the point where a macroscopic crack started to propagate in the test specimen. This can be compared with Fig. 3a where two distinct phases of the true stress-strain relationship can be seen after necking: first a slow increase of the stress that then accelerates towards the final fracture when the macroscopic crack occurs and propagates. The two curves "linear" and "bilinear" damage evolution (DE) in Fig. 12a were obtained by FE simulations, and Fig. 12b gives their definitions. The FE simulations were interrupted at a point that had a similar definition as the experimental point of interruption of a test, i.e. when the gradient of the stress-strain relation increased rapidly and fracture occurred. The displacement at fracture, u_f, used in the FE simulations was calculated using ε_f according to Barba's law, see Eq. (1).

Fig. 12: (a) Simulated tensile tests using a linear and a piecewise linear law for damage evolution (DE). Note that the solid line representing the experiments and the dash-dotted line representing the FE simulations using the bilinear damage evolution coincide. **(b)** Illustration of linear and piecewise linear DE relationships during the process of damage evolution.

In Fig. 12a, the results obtained by FE simulations using the model with linear damage evolution show a deviation in stress-strain behaviour at the point of necking in comparison with the experimentally obtained results. It may also be noted that it cannot mimic the damage process and seems to underestimate the energy released during the damage process. This could be remedied if the damage variable, D, is allowed to evolve according to a bilinear relationship, the results of which are shown in Fig. 12b. However, when defining such a relationship, the D-u_f relation has to be calibrated so that it results in the same amount of dissipated energy in order to reach zero stiffness at the same strain as the linear damage formulation, as can be seen in the illustration of the damage evolution in Fig. 12b. Using the bilinear damage evolution relationship, a calibrated value of the x-parameter to 0.2 resulted in excellent agreement with the experimentally obtained stress-strain curves, shown in Fig. 12a. A slower development of damage in the early phase and a more rapid evolution towards final fracture shows a closer resemblance to the two phases of the experimental observations leading to macroscopic crack initiation and propagation, as discussed above. This behaviour of acceleration towards final fracture was also observed in the FE simulation using the linear DE, but, in this particular case, it had to be enhanced using a bilinear law to match the test results.

Fig. 13 shows a comparison in results between a tensile test and an FE simulation of it. Fig. 13a shows the major principal strain in the facets on the specimen's surface, which was calculated using the data recorded by the ARAMIS measurement system. The corresponding result from an FE simulation is shown in Fig. 13b, in which the bilinear damage evolution relationship was used with $x = 0.2$. The results are presented at the time, T, which is 95% of the total time to fracture, T_f. There is very good agreement in results between the experiment

and the FE simulation with respect to magnitude of the major principal strain and the contours of its distribution.

(b)

Fig. 13: Major principal strain results for a tensile test presented at $T = 0.95T_f$: **(a)** results from an experiment using the ARAMIS system and **(b)** results from an FE simulation using Abaqus/Explicit.

6.2 Finite element simulations of forming limit tests

In the FE simulations of the forming limit tests all six geometries in Fig. 4a were assessed. To define damage initiation, which represented the necking in the experiments, the FLD criterion in Abaqus/Explicit was used with tabular values of ε_1 and ε_2 taken from the BWH curve presented in Fig. 11 as input. Degradation due to evolution of damage was represented in the FE model using the bilinear damage evolution law used also in the FE simulation of the tensile test ($x = 0.2$) (see Fig. 12b). The results from the FE simulations were evaluated similarly to the evaluation of tests; Section 4 presents details regarding this method.

The results presented in Fig. 14 show that the trends of both the necking and fracture are captured by the FE simulated values; however, some discrepancies are present. The points representing necking for the test geometries 2-6 are collected around the major principal strain axis, while the corresponding simulated points are more separated in the ε_1-ε_2 space. A similar trend can be seen with the points representing fracture. One reason for this effect may be that, as was discussed in Section 4, the material of the specimens was pre-strained (and anisotropic), which was not represented in the FE material model.

Fig. 14: Results presented in principal strain space from the experiments and FE simulations of the forming limit tests.

Fig. 15 shows a comparison in results of the major principal strain in a test specimen of geometry 2 and the FE simulation of the same geometry. The results are presented at a time, T, which is 95% of the total time to fracture, T_f. There is very good agreement in results both with respect to magnitude of the major principal strain and the contours of its distribution.

Fig. 15: Major principal strain results for a FLD test on geometry 2 at $T = 0.95T_f$: **(a)** results from an experiment using the ARAMIS system and **(b)** results from an FE simulation using Abaqus/Explicit.

7. Discussion

This investigation presents an experimental and numerical investigation on necking and fracture behaviour of sheet metals on a small scale, i.e. on specimens. Depending on the type of application and objective of the FE analysis, one may use either necking or fracture as the definition of failure in the analysis. Also, the sizes of the elements forming the model have to be adjusted in combination with the selected interruption criterion for element removal or damage evolution. In large structures like ships, large sizes of the elements that form the mesh are recommended in order to save computational efforts. Then, necking may be a sufficient criterion for failure and element removal, and it has been successfully used by, among others, Alsos [17, 18], who utilised the BWH criterion for this purpose. Marciniak et al. [19] also consider necking to be the point of failure, since the load carrying capacity of a structure consisting of sheet material is lost after the point of necking.

Even though the BWH instability criterion used in the current investigation is based on numerous assumptions concerning the mechanisms involved in necking of sheet metal, the procedure for adapting the criterion to experimental values [1] gives a good correlation with the results from the forming limit tests. Furthermore, using this criterion within the FE analysis of the forming limit tests captures the trend of the experimental values for necking. The discrepancy between experimental and simulated values may be explained by the pre-straining and anisotropy of the tested material, an effect which was not accounted for in the material description of the FE models in the present study.

In future work, the model of failure established within the current investigation will be incorporated into large scale FE simulation of ship-to-ship collisions, an example of which is shown in Fig. 16. In Abaqus/Explicit, the FLDCRIT variable is used as a measure to present the initial accumulation of damage of the material between the yielding point, FLDCRIT = 0, and the point of necking, FLDCRIT = 1 if the FLD-criterion is used. The SDEG variable shows the evolution of damage in an element between the necking point, SDEG = 0, and fracture, SDEG = 1. When SDEG = 1, the elements are removed from the mesh to visualize if, for example, a crack/hole has occurred in the side-shell of the ship, as seen in Fig. 16a. Fig. 16b shows the result from the same analysis and time step as in Fig. 16a but for the SDEG variable. It should be noted that in this type of simulation, many different sizes of elements will be used in order to resolve the ship structure appropriately. In that way, the failure behaviour dependence on element size established in experiments and FE analysis of the tensile test, like in Figs. 2 and 12, should be used. On the other hand, the elements will most likely be of such a size that their failure strain is close to the global strain of the tensile test, cf. the asymptotic relations in Figs. 3b, 3d and 3f, in which case this global failure strain will be used. However, in failure analysis of other applications where smaller elements are used,

this dependence will have a large impact on the solution and should be compensated for. Also, it is beneficial to have a law of damage evolution when conducting FE analysis using Abaqus/Explicit, since this mitigates numerical instabilities that may occur if large stiffness gradients are present in the solution. Furthermore, the geometry of a ship structure consists of large plates (cf. forming limit test geometry 1 in Fig. 5a) and narrow stiffeners (cf. forming limit test geometries 2-6 in Fig. 4a) in which very different stress states will be present. In FE analysis, this will be compensated for by using the FLD criterion for damage initiation in Abaqus/Explicit with input data from the analytical solution of the BWH instability relation fitted to experimental data.

Fig. 16: Example of results from an FE simulation of a ship-to-ship collision event. Part of the side shell of the struck ship is shown here without the bow of the striking ship: **(a)** result that presents when the criterion for fracture is reached by the SDEG variable, and **(b)** the corresponding magnitude of the FLDCRIT variable, which is a measure of how close to the point of necking the remaining elements of the mesh are; see the text for details. The elements that have been removed from the mesh have reached full damage, i.e. SDEG = 1.

8. Conclusions

A methodology is proposed that details how to model the failure behaviour of a material in terms of length scale and multiaxiality in FE simulations. It is shown that this methodology can capture the trends of the experiments. The results from the tensile tests show consistency in the comparison between different definitions of necking. Applying the definition of necking as a localization of deformations on the forming limit tests makes it possible, through the accurate data on surface strains recorded by the ARAMIS system, to determine where necking occurs for these tests as well.

A method to identify the point of instability in sheet metal through this definition of necking is proposed for forming limit tests. Concerning the post-necking behaviour of the material, this was modelled in FE simulations using a bilinear law for damage evolution found through observations on tensile tests. The same evolution law was applied to the FE simulations of the forming limit tests which then correlate well with the trends in the experiments.

The method presented in Alsos et al. [1] to apply the BWH criterion to experimental values of necking at the forming limit tests showed good agreement between test values and those predicted by the criterion. In terms of using the FLD criterion in Abaqus/Explicit, with input from the BWH criterion adapted to the experimental points of necking and the damage evolution found in the tensile tests, the results from the simulations capture the trend of the experimental necking and fracture FLCs well. In the comparison of the results from the tests and the FE simulations of the forming limit test geometries 2 to 6 (see Sections 4 and 6.2), the results from the FE simulations are more separated in the ε_1-ε_2 space in contrast to the test results. This difference can be explained by the pre-strain and anisotropy that is caused by the manufacturing process of the material tested—an effect which was not incorporated in the description of the material characteristics in the FE model.

Acknowledgements

This investigation has been carried out as part of the research project HASARD (Holistic assessment of ship survivability and risk after damage). The authors acknowledge the Swedish Governmental Agency of Innovation Systems (VINNOVA) and the Swedish Competence Centre in Maritime Education and Research, LIGHTHOUSE (www.lighthouse.nu), for financing the project. The authors are also grateful to the staff at the division of Building Technology and Mechanics at SP Technical Research Institute of Sweden in Borås, Sweden for providing expertise and support in conducting the experiments.

References

1. Alsos HS, Hopperstad OS, Törnqvist R, Amdahl J. Analytical and numerical analysis of sheet metal instability using a stress based criterion. International Journal of Solids and Structures 2008;45:2042-2055.
2. Karlsson U, Ringsberg JW, Johnson E, Hosseini M, Ulfvarson A. Experimental and numerical investigation of bulb impact with a ship side-shell structure. Accepted for publication in Marine Technology 2008 (In press).
3. Hong L, Amdahl J, Alsos HS, Klaebo F. Damage assessment and impact resistant design of FPSOs with respect to supply vessel collisions. In: Basu RI, Belenky V, Wang G and Yu Q. editors. Proceedings of the 10th International Symposium on Practical Design of Ships and Other Floating Structures Houston, Texas, U.S.A. (PRADS 2007): 2007. p. 622-630.
4. ARAMIS. http://www.gom.com/EN/measuring.systems/aramis/ (2008-12-03).
5. Lehmann E, Peschmann J. Energy absorption by the steel structure of ships in the event of collisions. Marine Structures 2002;15:429-441.

6. Ramaekers JAH. A criterion for local necking. Journal of Materials Processing Technology 2000;103:165-171.

7. Ragab AR. Prediction of fracture limit curves in sheet metals using a void growth and coalescence model. Journal of Materials Processing Technology 2008;199:206-213.

8. Zhao L, Sowerby R, Sklad M P. A theoretical and experimental investigation of limit strains in sheet metal forming. International Journal of Mechanical Sciences 1996;38;12:1307-1317.

9. Stoughton T B, Zhu X. Review of theoretical models of the strain-based FLD and their relevance to the stress-based FLD. International Journal of Plasticity 2004;20:1463-1486

10. Det Norske Veritas (DNV). Rules for classification of ships/high speed, light craft and naval surface craft. 2007.

11. SSAB. http://www.ssabdirekt.com/upload/dokument/Datasheets/GB/Domex/GB8413Domex.pdf. (2008-12-03).

12. ISO 12004-2. Metallic materials-Sheet and strip-Determination of forming limit curves-Part 2: Determination of forming limit curves in laboratory. 2007.

13. Dowling NE. Mechanical Behaviour of Materials 3rd edition. Pearson Prentice Hall, Upper Saddle River, NJ, U.S.A., 2007.

14. Yamada Y, Endo H, Terndrup-Pedersen P. Numerical study on the effect on buffer bow structure in ship-ship collision. In: Proceedings of the 15th International Offshore and Polar Engineering Conference 2005, Seoul, Korea: 2005. p. 604-611.

15. Hill R. On discontinuous plastic states, with special reference to localized necking in thin sheets. Journal of the Mechanics and Physics of Solids 1952;1:19-30.

16. Dassault Systèmes. Abaqus version 6.7 documentation. 2007.

17. Alsos H S, Amdahl J, Hopperstad O S. On the resistance to penetration of stiffened plates, Part I – Experiments. International Journal of Impact Engineering, 2009;36:799-807

18. Alsos H S, Amdahl J, Hopperstad O S. On the resistance to penetration of stiffened plates, Part II: Numerical analysis. International Journal of Impact Engineering, 2009;36:875-887

19. Marciniak Z, Duncan JL, Hu SJ. Mechanics of Sheet Metal Forming, Butterworth-Heinemann, Oxford, U.K., 2002.

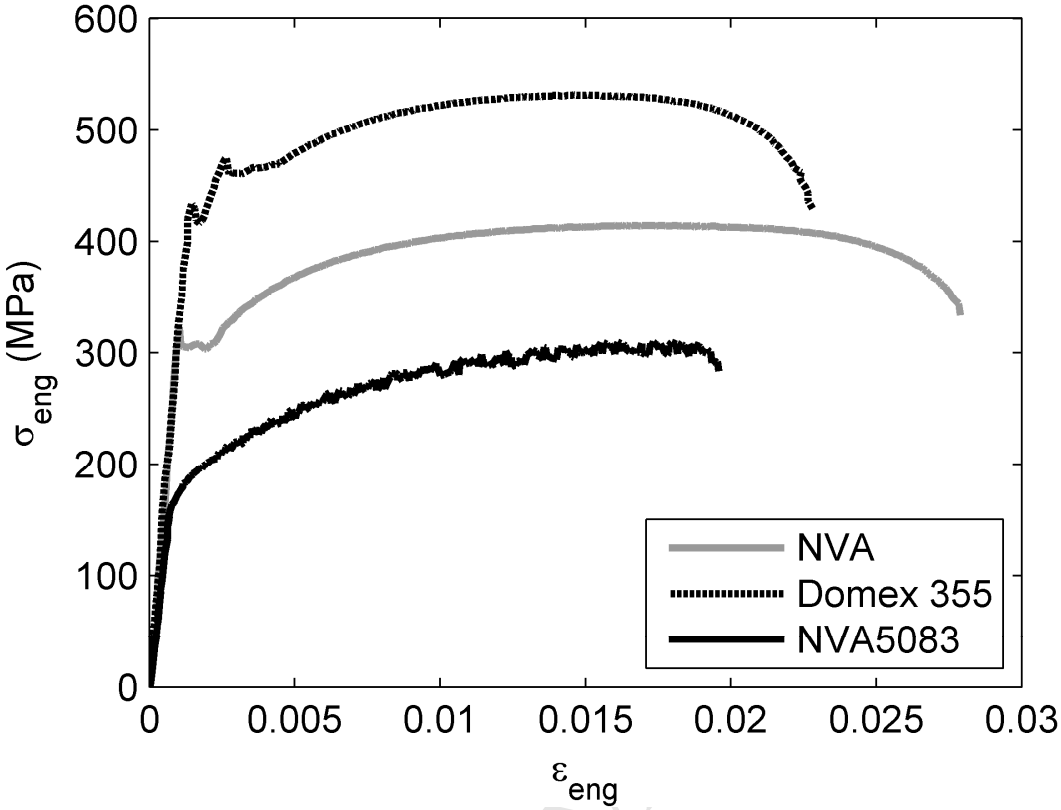

Fig. 1: Typical engineering stress-strain curves for the tested materials, NVA, Domex 355 and NV5083

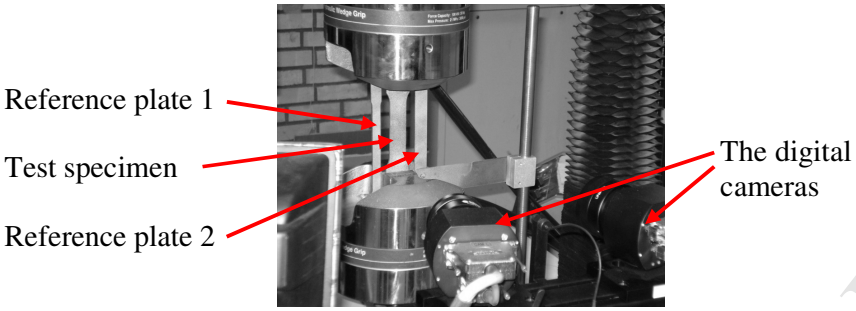

Fig. 2: Test setup for the tensile test.

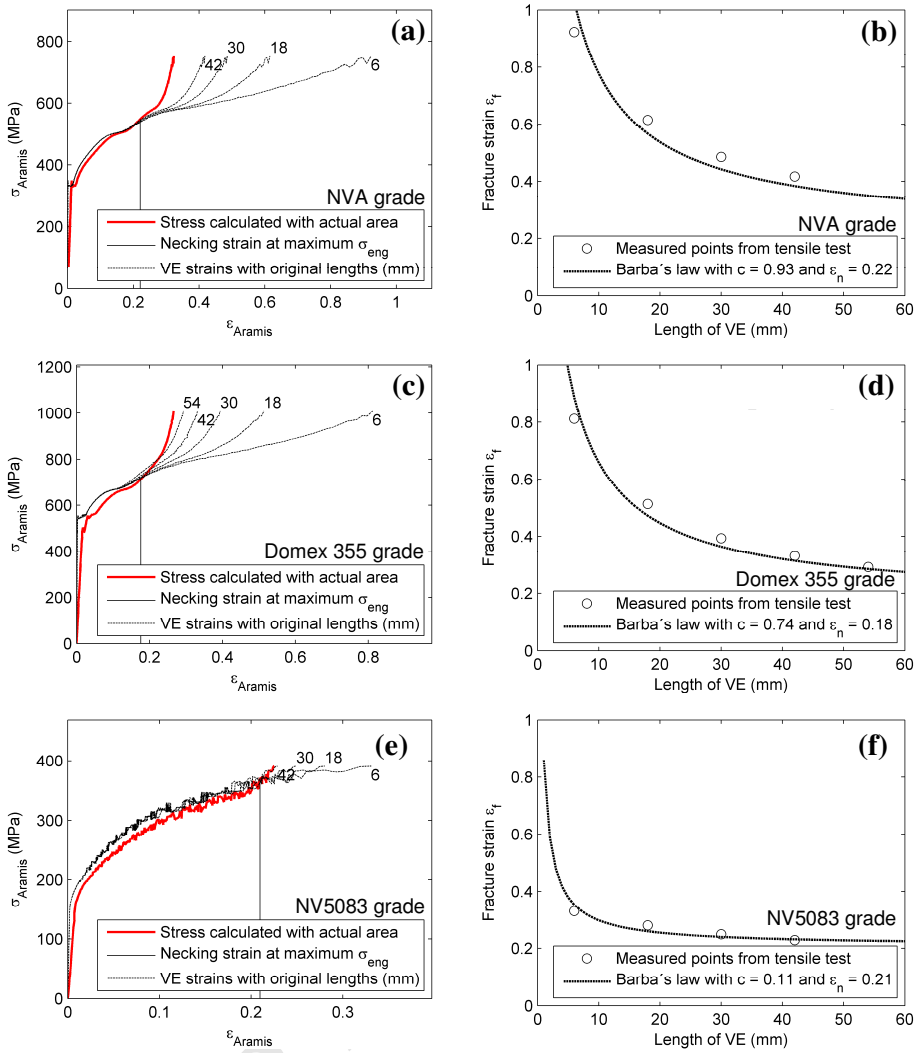

Fig. 3: Results from the tensile tests where the stress is calculated based on the actual area of the test specimen, and the strain is measured in accordance with the length of the virtual extensometer (given in mm): **(a)** the NVA material, **(c)** the Domex 355 material and **(e)** the NV5083 material. Presentation of the fracture strain as a function of the length of the virtual extensometer together with Barba's relation fitted to the measured points. **(b)** the NVA material, **(d)** the Domex 355 material and **(f)** the NV5083 material.

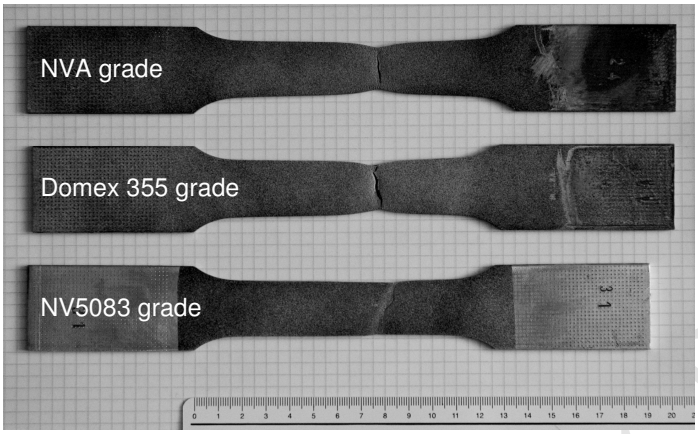

Fig. 4: Three tensile test rods after testing which are made of the NVA, the Domex355 and the NV5083 grade materials.

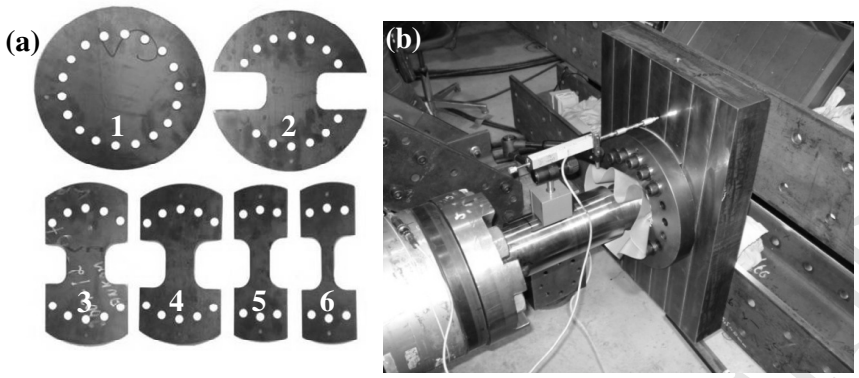

Fig. 5: (a) The six test geometries: each of them corresponds to one strain state in the forming limit diagram. Geometry 1 is the circular plate (upper left) and geometry 6 is the narrowest of the geometries (lower right). **(b)** Test setup: the punch goes into the hold in which the specimen is clamped, the Teflon lubrication sheets can be seen between them. Also, the displacement gauge can be seen fixed on top of the punch.

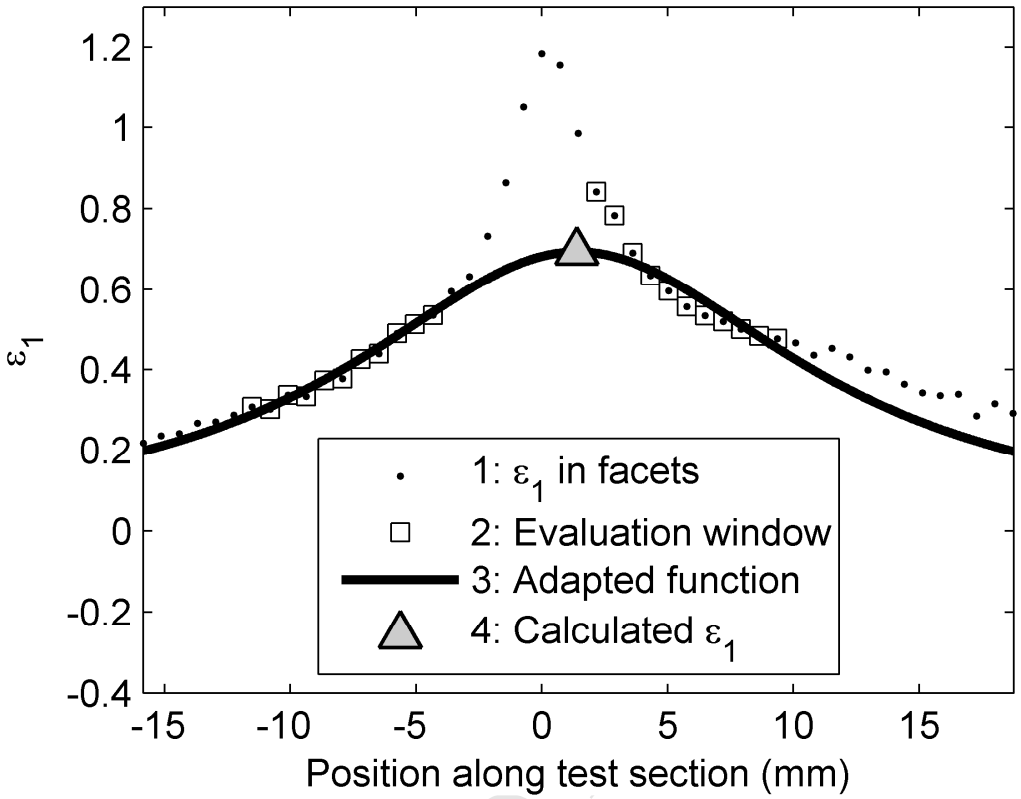

Fig. 6: Example of evaluation procedure of the forming limit test results in accordance with ISO 12004-2 [10] to obtain the major principal strain, ε_1, in one of the five evaluation sections of a test specimen. The position 0 along the test section (x-axis) corresponds to the location of the crack.

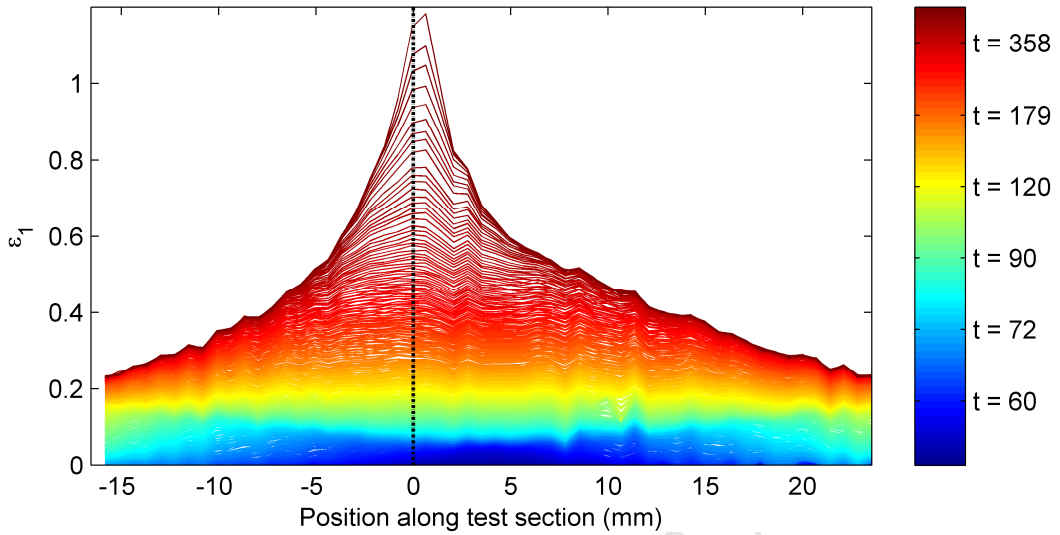

Fig. 7: Example of a presentation of the evolution in time of the major principal strain in one section of a test geometry. The dashed line indicates where in the specimen localization is expected to occur.

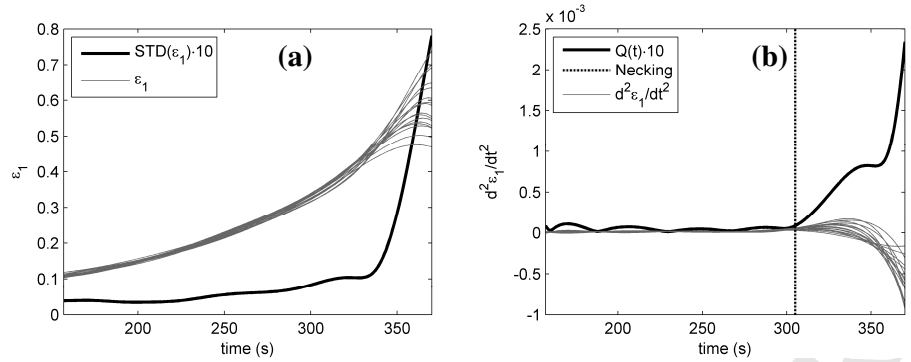

Fig. 8: (a) Curves for the major principal strain history in the points of the evaluation window (see squares in Fig. 5) and their standard deviation enhanced by a factor of 10. **(b)** Major principal strain acceleration of the curves in (a) and their standard deviation enhanced by a factor of 10. The dashed line indicates necking.

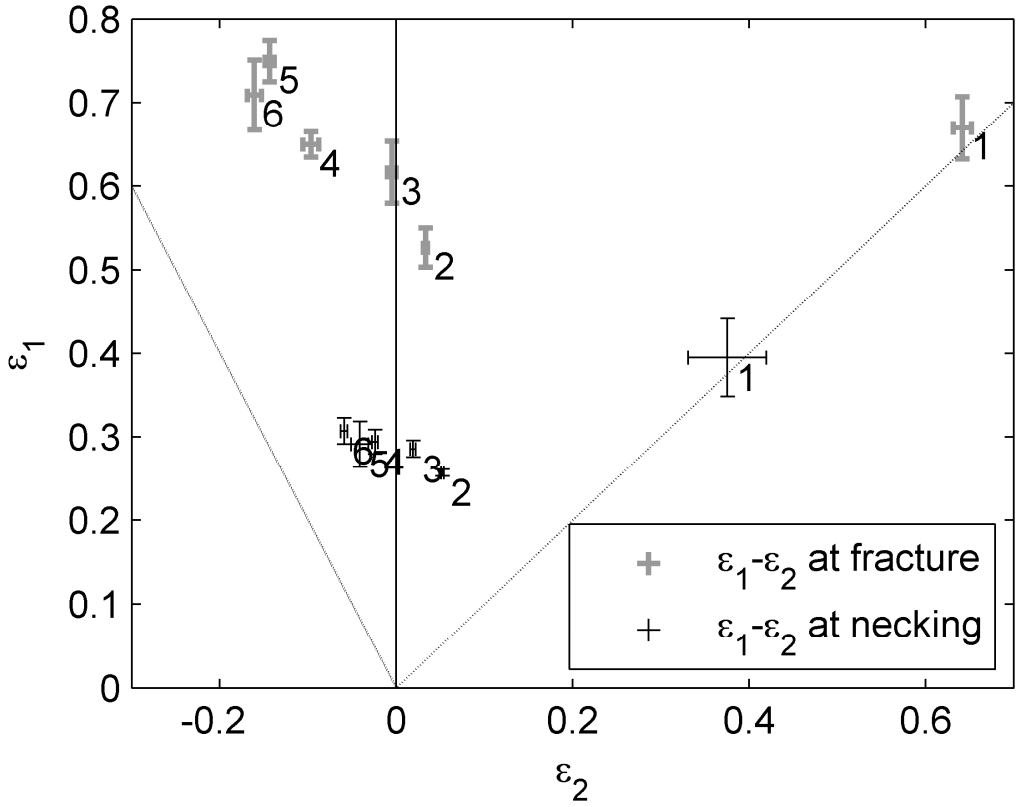

Fig. 9: Results from forming limit tests of the six geometries (based on five sections on three test samples for each geometry): mean values and standard deviations (denoted by the error bars) in the principal strain space (ε_1 and ε_2 directions), for necking and fracture.

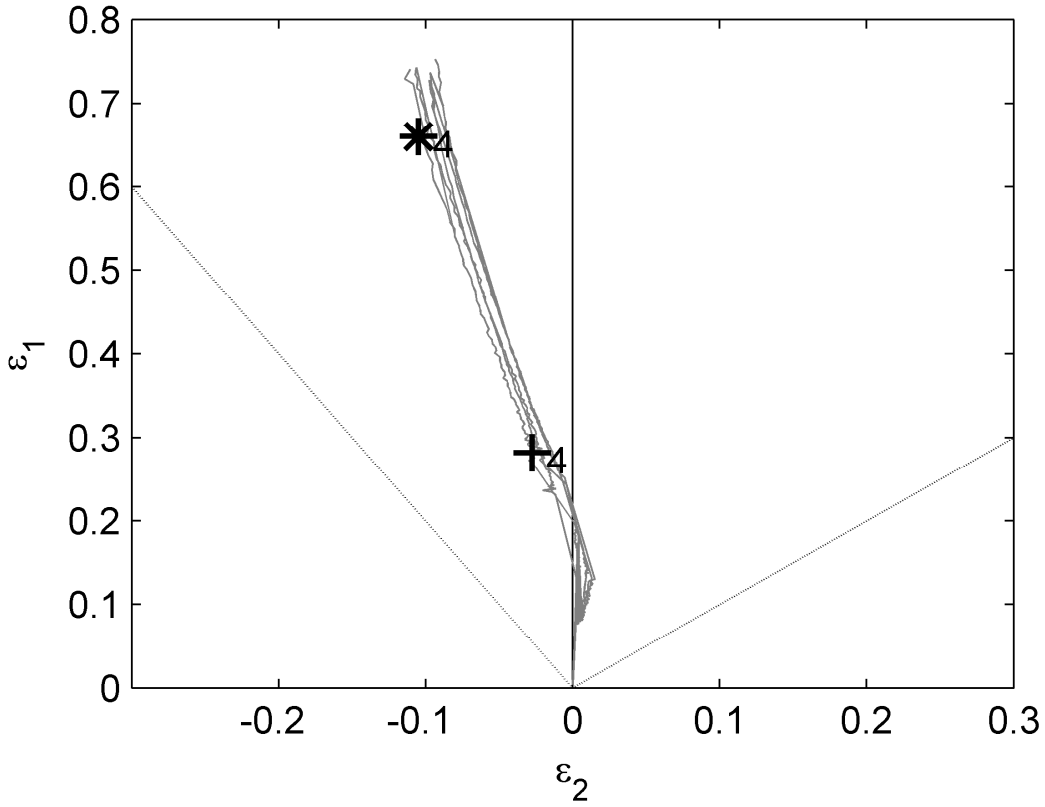

Fig. 10: Strain path during the forming limit tests for five sections of one test specimen geometry 4.

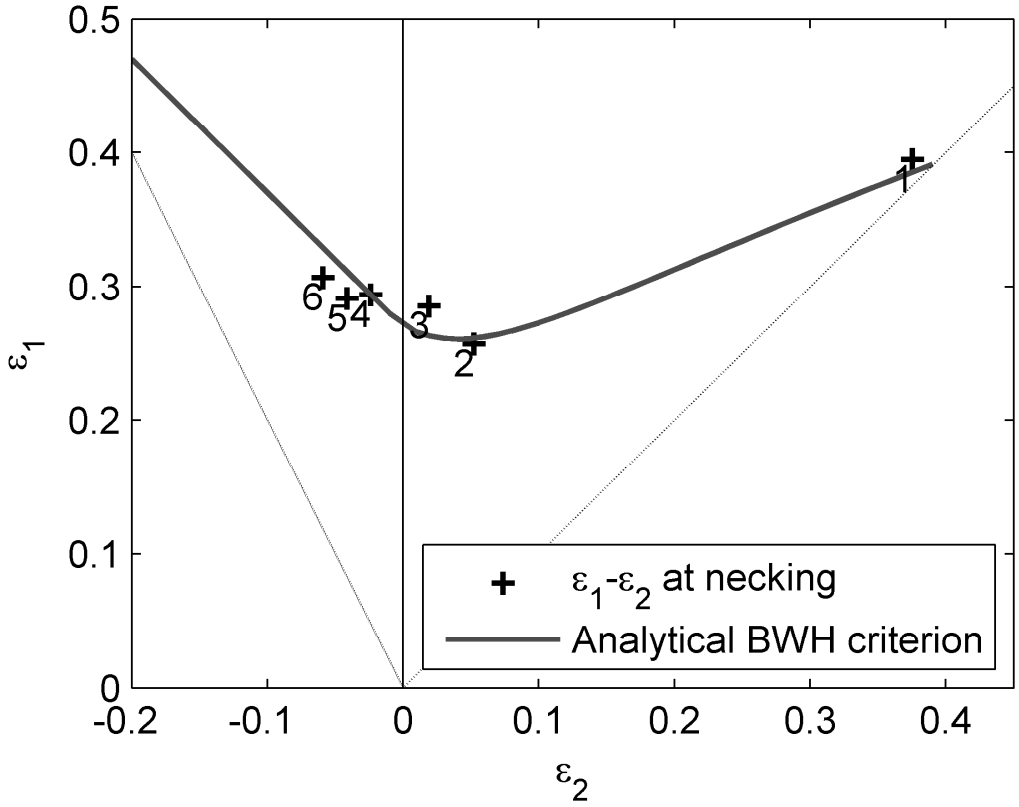

Fig. 11: Results (necking) from forming limit tests together with the analytical solution of the BWH criterion fitted to the experimental values presented in principal strains.

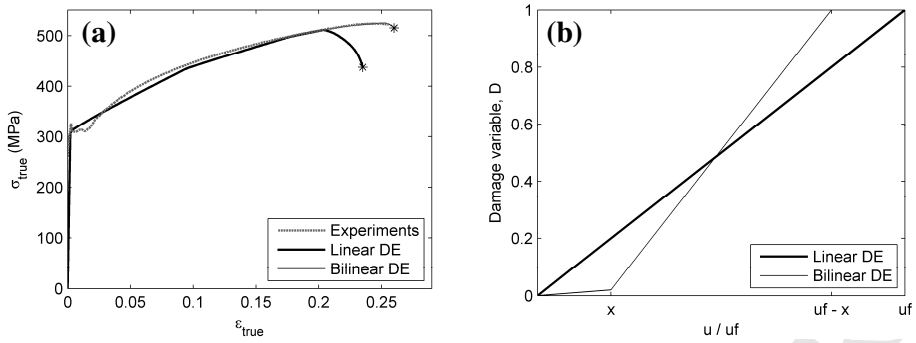

Fig. 12: (a) Simulated tensile tests using a linear and a piecewise linear law for damage evolution (DE). Note that the solid line representing the experiments and the dash-dotted line representing the FE simulations using the bilinear damage evolution coincide. **(b)** Illustration of linear and piecewise linear DE relationships during the process of damage evolution.

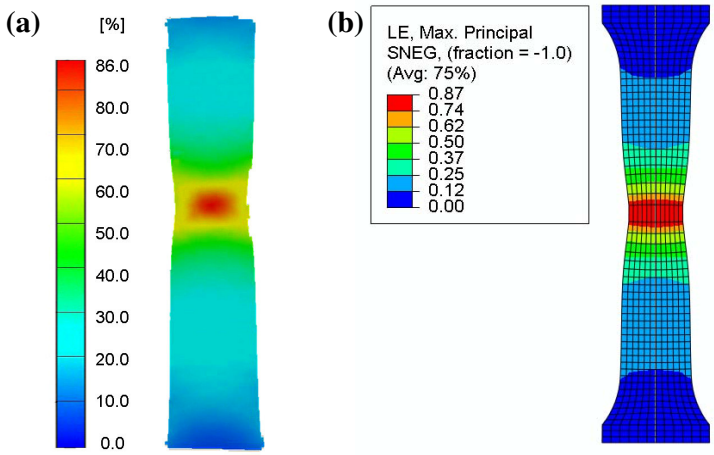

Fig. 13: Major principal strain results for a tensile test presented at $T = 0.95T_f$: **(a)** results from an experiment using the ARAMIS system and **(b)** results from an FE simulation using Abaqus/Explicit.

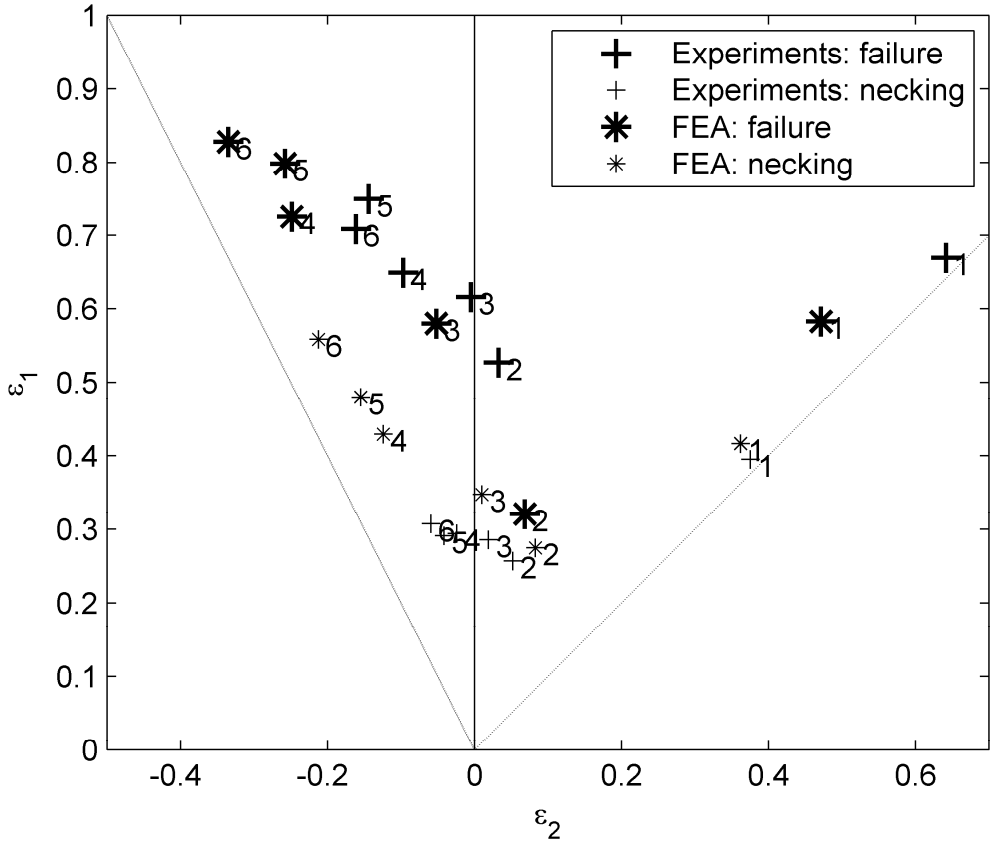

Fig. 14: Results presented in principal strain space from the experiments and FE simulations of the forming limit tests.

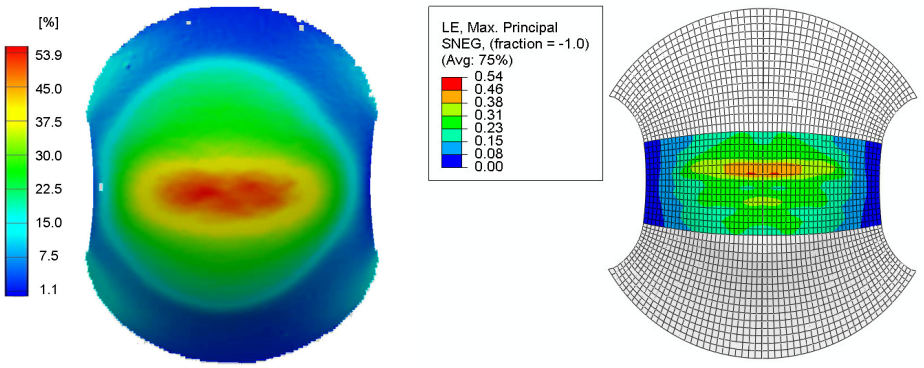

Fig. 15: Major principal strain results for a FLD test on geometry 2 at $T = 0.95T_f$: **(a)** results from an experiment using the ARAMIS system and **(b)** results from an FE simulation using Abaqus/Explicit.

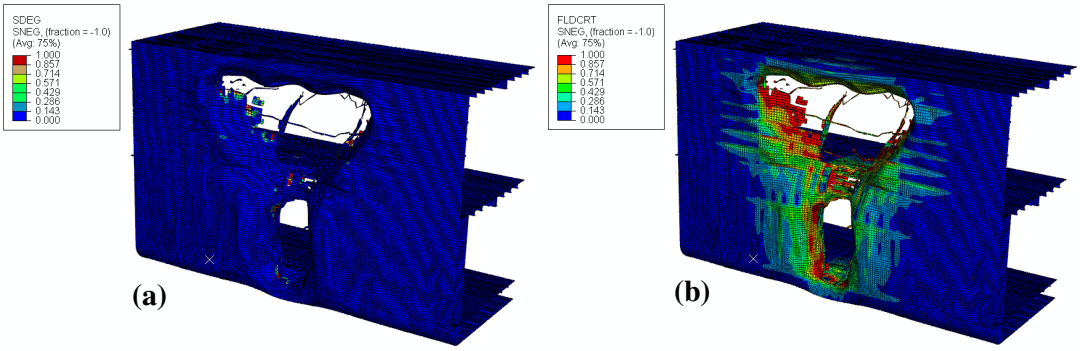

Fig. 16: Example of results from an FE simulation of a ship-to-ship collision event. Part of the side shell of the struck ship is shown here without the bow of the striking ship: **(a)** result which presents when the criterion for fracture is reached by the SDEG variable, and **(b)** the corresponding magnitude of the FLDCRIT variable which is a measure of how close to the point of necking the remaining elements of the mesh are; see the text for details. The elements that have been removed from the mesh have reached full damage, i.e. SDEG = 1.